RESEARCH PAPER

A. J. Kulkarni · M. Zhou

Surface-effects-dominated thermal and mechanical responses of zinc oxide nanobelts

Abstract Molecular dynamics (MD) simulations are carried out to characterize the mechanical and thermal responses of [01$\bar{1}$0]-oriented ZnO nanobelts with lateral dimensions of 21.22 Å × 18.95 Å, 31.02 Å × 29.42 Å and 40.81 Å × 39.89 Å over the temperature range of 300-1000 K. The Young's modulus and thermal conductivity of the nanobelts are evaluated. Significant surface effects on properties due to the high-surface-to-volume ratios of the nanobelts are observed. For the mechanical response, surface-stress-induced internal stress plays an important role. For the thermal response, surface scattering of phonons dominates. Calculations show that the Young's modulus is higher than the corresponding value for bulk ZnO and decreases by ∼33% as the lateral dimensions increase from 21.22 Å × 18.95 Å to 40.81 Å × 39.89 Å. The thermal conductivity is one order of magnitude lower than the corresponding value for bulk ZnO single crystal and decreases with wire size. Specifically, the conductivity of the 21.22 Å × 18.95 Å belt is approximately (31-18)% lower than that of the 40.81 Å × 39.89 Å belt over the temperature range analyzed. A significant dependence of properties on temperature is also observed, with the Young's modulus decreasing on average by 12% and the conductivity decreasing by 50% as temperature increases from 300 K to 1000 K.

Keywords Zinc oxide nanobelts · Surface effects · Size dependence · Young's modulus · Thermal conductivity

1 Introduction

Zinc oxide (ZnO) nanobelts are one class of nanostructures endowed with semiconductivity, piezoelectricity and coupled

A. J. Kulkarni · M. Zhou (✉)
The George W. Woodruff School of Mechanical Engineering,
Georgia Institute of Technology, Atlanta,
Georgia 30332-0405, USA
E-mail: min.zhou@me.gatech.edu

thermomechanical responses [1]. As functional nano-building blocks, these components have a wide variety of potential applications such as catalysts, chemical sensors, resonators, transparent conductors, biosensors, medical devices, nano-electronic components, and nano-photonic components [2–11]. The mechanical and thermal behaviors of these nanocomponents are important in many of the applications since strength, stiffness, and thermal conductivity are among the key attributes involved. For example, the assembly of nanobelts between electrodes or substrates in a system requires a balance of rigidity and strength. The mechanical response of nanocomponents is also of critical importance because in applications such as nanocantilever sensors the mechanical resonance depends on the bending modulus. On the other hand, at the nanoscale, electric field density and heat flux are very high and are therefore of great concern. One example involves thermoelectric applications which require careful control of the thermal and electrical conductivities. A great challenge and perhaps also an opportunity in regulating such properties for device integration is their dependence on size on the nanoscale. The primary contributor to this size effect is the high surface-to-volume ratios in the 1D nanostructures. Unlike on the macroscale where the effect of surfaces on material response is negligible due to very low surface-to-volume ratios, surfaces play a dominant role in altering the behavior on the nanoscale. The size dependences of Young's moduli and thermal conductivity are examples [12,13]. Characterization of such property variations with size is therefore very important.

Since the nanobelts have only been synthesized recently, there is a lack of understanding and characterization of their mechanical and thermal behaviors. Outstanding scientific and technical issues include the quantification of constitutive behavior (including strength, moduli and ductility), size and temperature dependence of behavior, thermal conductivity and phase transformations. In this paper, the response to quasi-static tensile loading and thermal excitation of [01$\bar{1}$0]-oriented ZnO nanobelts with cross-sections of 21.22 Å × 18.95 Å, 31.02 Å × 29.42 Å and 40.81 Å × 39.89 Å are characterized over the temperature range of 300-1000 K. The

Young's modulus and thermal conductivity are obtained as functions of lateral dimensions and temperature. The dominating effects of surfaces on both the mechanical and thermal responses are analyzed.

2 Framework of analysis

The as-synthesized nanobelts are single-crystalline and wurtzite-structured with lattice constants $a = 3.249$ Å and $c = 5.206$ Å. Their thickness is between 5–20 nm with typical width-to-thickness ratios of 5-10 [14]. The belt structure can be obtained by repeating the unit wurtzite cell along the $[01\bar{1}0]$ growth direction, as shown in Fig. 1. The minimum cross-sectional size analyzed (21.22 Å × 18.95 Å) is chosen such that the short range cutoff distance is smaller than the smallest belt dimension and long-range interactions are properly considered. Periodic boundary conditions (PBCs) are specified in the axial direction to approximate the behavior of long belts. A small periodic length can significantly affect the calculated thermal responses by introducing image effects since PBCs effectively truncate the phonon wavelength spectrum. Calculations show that any length above 100 Å is sufficient for avoiding such image effects [15]. The simulation cell is therefore chosen as 150 Å in the axial direction and cross-sectional dimensions of 21.22 Å × 18.95 Å, 31.02 Å × 29.42 Å and 40.81 Å × 39.89 Å are used to evaluate the size effect.

The atomic interactions are modeled using a Buckingham potential with charge interactions [16,17] of the form

$$\phi(r_{ij}) = \frac{q_i q_j}{4\pi\varepsilon_0 r_{ij}} + A\exp\left(\frac{-r_{ij}}{\rho}\right) - \frac{C}{r_{ij}^6}, \tag{1}$$

where ε_0 is the permittivity of free space, r_{ij} is the distance between ions i and j, q_i is the charge on ion i and A, ρ

and C are potential parameters whose values are given in Ref. [17]. The short range parameters in the second and the third terms are fitted to the structure and properties of ZnO using quantum-mechanical and classical methods. The electrostatic interactions in the first term are summed using the Wolf method which significantly reduces computational time [18,19].

After geometric construction, the nanobelts are first equilibrated at the desired temperature for 10 ps with traction free boundary conditions. Approximation to quasi-static tensile loading in each deformation increment is achieved in two steps. First, a velocity of 1 Å/ps (ramped from 0) is applied to boundary atoms A in Fig. 2 to effect extension up to a displacement of ∼0.3 Å. This is followed by equilibration of the entire structure for 3ps with boundary atoms fixed at their current positions. This results in a nominal strain of 0.3% per deformation increment. The virial formula is used to calculate the stress [20]. The Young's modulus is obtained from the slope of the linear portion of the stress-strain curve.

Evaluation of the thermal conductivity uses the Green-Kubo approach which is based on the fluctuation-dissipation theorem. Specifically, the thermal conductivity is written as

$$\lambda_{\mu\nu} = \frac{1}{Vk_B T^2} \int_0^\infty \langle J_\mu(t)J_\mu(0)\rangle \mathrm{d}t, \tag{2}$$

where V is system volume, T is temperature, k_B is Boltzmann constant, $J_\mu(t)$ is the μth ($\mu = 1, 2, 3$) component of the heat current $\boldsymbol{J}$ and $\langle J_\mu(t)J_\mu(0)\rangle$ is the auto-correlation function for $J_\mu(t)$ with $\langle\ \rangle$ denoting ensemble time average. The heat current is calculated as

$$\boldsymbol{J}(t) = \sum_{i=1}^{N}\left(\boldsymbol{v}_i E_i + \frac{1}{2}\sum_{j=1, j\neq i}^{N}\boldsymbol{r}_{ij}(\boldsymbol{F}_{ij}\cdot\boldsymbol{v}_i)\right), \tag{3}$$

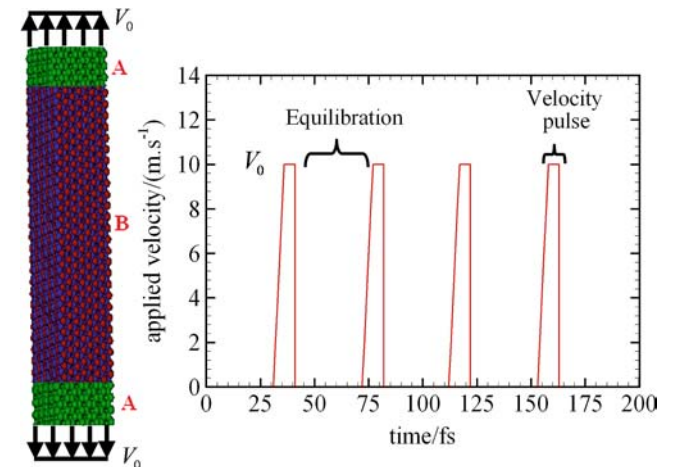**Fig. 1** (a) Unit wurtzite cell; (b) Nanobelt assembled in the $[01\bar{1}0]$ growth orientation

Fig. 2 Quasi-static loading scheme dipicting the applied velocity pulse and the intermediate equilibration steps. The velocity boundary condition is applied to the boundary atoms (sections A, colored green). Section B is the gauge length

where $\boldsymbol{r}_i$, $\boldsymbol{v}_i$ and E_i are the position vector, velocity and total energy of atom i, respectively; $\boldsymbol{r}_{ij} = \boldsymbol{r}_j - \boldsymbol{r}_i$ and $\boldsymbol{F}_{ij}$ is the force exerted on atom i by atom j. The first term in Eq. (3) represents the convection contribution to heat flow. This term is inconsequential in solids and is ignored in conductivity calculations.

The upper limit for the integral in Eq. (2) extends to infinity since theoretically the time required for a system to attain thermal equilibrium tends to infinity. To calculate thermal conductivity in a realistic manner, however, the integral is truncated after a certain time period which is defined as the delay time τ_m and the system is assumed to have reached equilibrium at that time. The choice of the delay time depends on the material system analyzed since it is a measure for a system's inherent thermal response. For the nanobelts here, the delay time is determined to be 2-5 ps (details later). To calculate thermal conductivity, for each delay time the autocorrelation function values are averaged over a number of time origins within the simulation window. Hence, the average measure of thermal conductivity can be expressed as a function of delay time as

$$\lambda_{\mu\nu}(\tau_m) = \frac{\Delta t}{V k_B T^2} \sum_{m=1}^{M} \frac{1}{N-m} \sum_{n=1}^{N-m} J_\mu(m+n) J_\nu(n), \quad (4)$$

where Δt is the simulation timestep, $N\Delta t$ is the total simulation time and the delay time $\tau_m = M\Delta t$.

The thermal analysis presented here is limited to temperatures near or above the Debye temperature $\theta_D (= 420\,\mathrm{K}$ for ZnO). Consequently, temperature can be calculated through mean kinetic energy and the theorem of equipartition of energy as

$$\frac{3}{2}Nk_B T = \frac{1}{2}\sum_{i=1}^{N} m_i v_i^2, \quad (5)$$

with N being the number of atoms in the system and m_i being the mass of atom i. Temperatures significantly below θ_D, for which quantum mechanical corrections may be needed, are not considered here.

3 Results and discussion

3.1 Surface structures

The nanobelts are dynamically relaxed with traction free boundary conditions to obtain their free-standing states. During equilibration, minimization of energy occurs through surface reconstruction and adjustment of the lattice spacing in the belt core. The surface reconstruction manifests in the forms of decreases in the interlayer spacing between outer surface layers and in-plane contractions of the surfaces. As shown in Fig. 3, the spacing between the two outermost layers of (000$\bar{1}$) planes and that between the two outermost layers of (2$\bar{1}\bar{1}$0) planes decrease by 73% and 9%, respectively, resulting in higher atomic densities in the surfaces compared to the belt core [12]. The surface reconstruction seen here
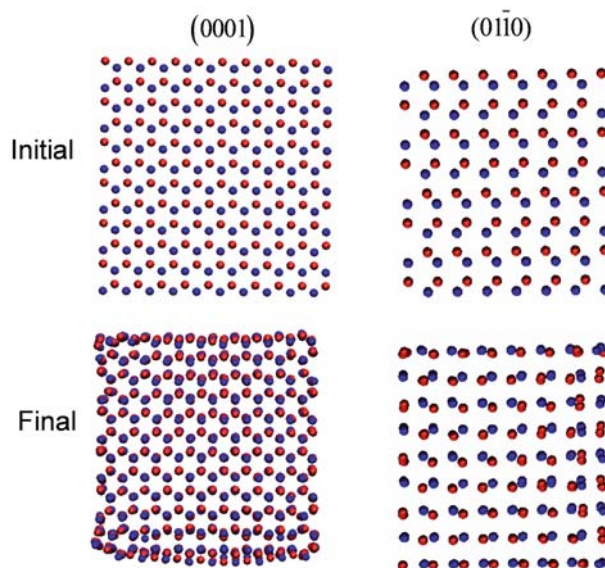

Fig. 3 Surface configurations for the nanobelts before and after equilibration. Reconstructions of (0001) and (2$\bar{1}\bar{1}$0) surfaces are observed

is a consequence of the reduced charge transfer and imbalance of ionic forces on the surfaces where atoms have fewer neighbors relative to those in the core. The reduced coordination of the surface atoms is also responsible for the in-plane relaxation of the surface atoms. As shown by Sander [21], the surface energy curve has a positive slope at zero surface strain, i.e., minimum surface energy occurs at a compressive surface strain. Consequently, in-plane contraction leads to a surface configuration considerably different from that in the bulk. Both effects become significant at small sizes since the surface-to-volume ratio increases with decreases in size. Specifically, as the size decreases from 50 Å to 10 Å, the fraction of surface atoms increases from 10% to 45% (see Fig. 4), indicating that an increasingly larger portion of atoms reside on the surface rather than in the interior. As a result of this,
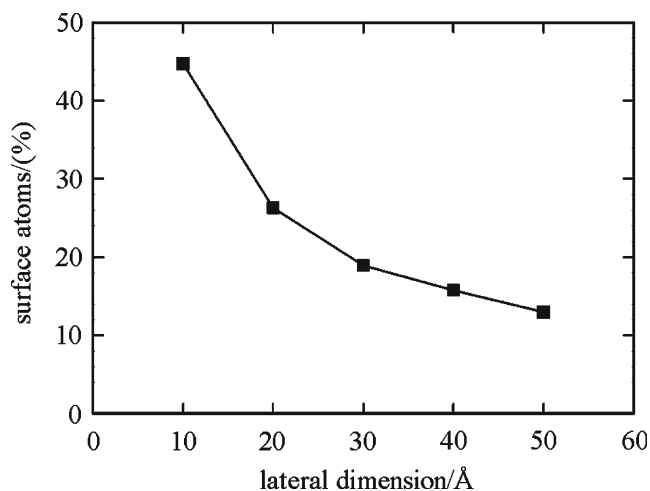

Fig. 4 Fractions of surface atoms as a function of lateral dimensions of the nanobelts

surface energy constitutes a major portion of the total configurational energy of the nanobelts and plays a significant role in determining the configuration of the nanobelts. Owing to their higher fractions, the behavior of surface atoms plays an increasingly dominant role in determining the thermal and mechanical behaviors of the nanobelts.

3.2 Mechanical response and effect of surface stress

To obtain their mechanical behavior, the nanobelts are subjected to uniaxial tensile loading. Figure 5 shows the response of a 21.22 Å × 18.95 Å belt at 300 K. The deformation occurs in three stages: initial elastic stretching, structural transformation from wurtzite-ZnO to simple hexagonal-ZnO, and eventual shear failure. The stress-strain relation is essentially linear in the elastic regime. Deformation beyond the elastic regime results in a stress drop from 4.6 GPa to 3.6 GPa. Such a softening behavior is indicative of the initiation of a phase transformation [22–28]. The transformation begins at a strain of 2.7% and as the deformation progresses the transformed region sweeps through the whole specimen. The transformation is completed at a strain of 6% and a stress of 6.2 GPa. The resulting structure is a metastable hexagonal phase ($a = 3.57$ Å, $c = 4.2986$ Å, Fig. 6). Similar transformations have been reported in inorganic and non-metallic materials, the most notable being a wurtzite-to-graphite trans-
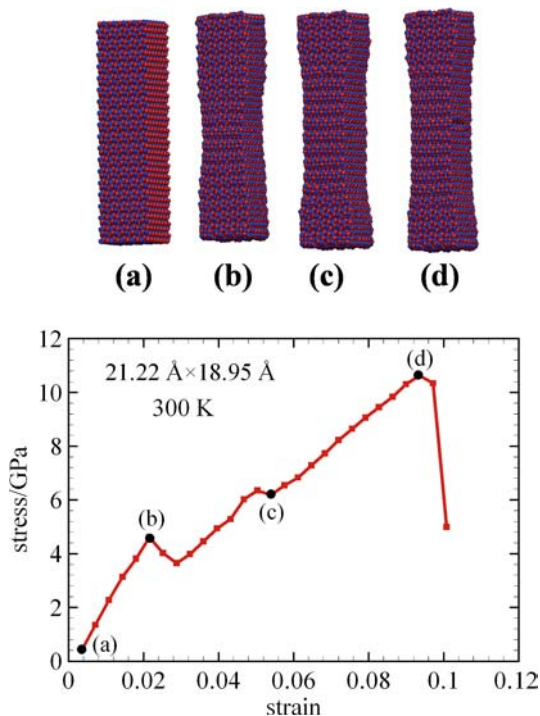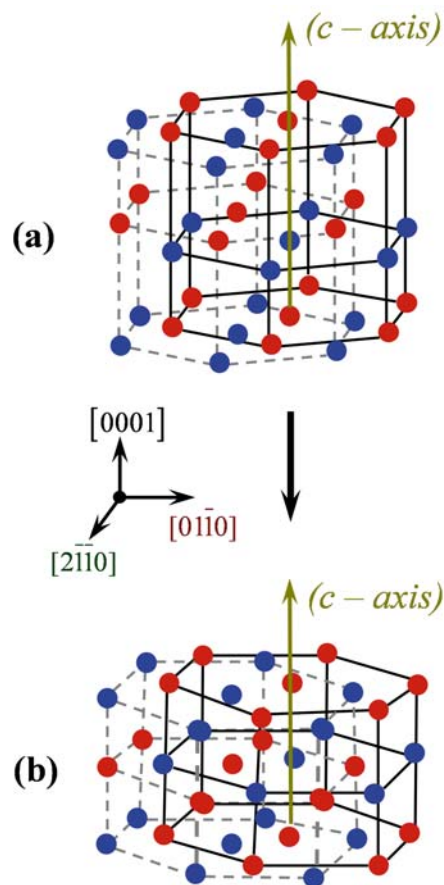

Fig. 6 An illustration of the structural transformation. (a) Initial wurtzite structure; (b) Final hexagonal phase

formation in boron nitride [26]. Further deformation involves the elastic stretching of the transformed structure and eventual failure at a strain of 7.2% and a stress of 15 GPa through cleavage along ($\bar{1}2\bar{1}0$) type planes.

Figure 7 shows the effect of lateral size on stress-strain response at 300 K. The Young's modulus of the nanobelts is

Fig. 5 Tensile stress-strain response for the 21.22 Å × 18.95 Å nanobelt. (a) Initial equilibrated state; (b) Nucleation of the structure transformation; (c) Completion of the transformation over the gauge length of the specimen with corresponding stress increase; (d) Failure by shear along ($\bar{1}2\bar{1}0$) type planes
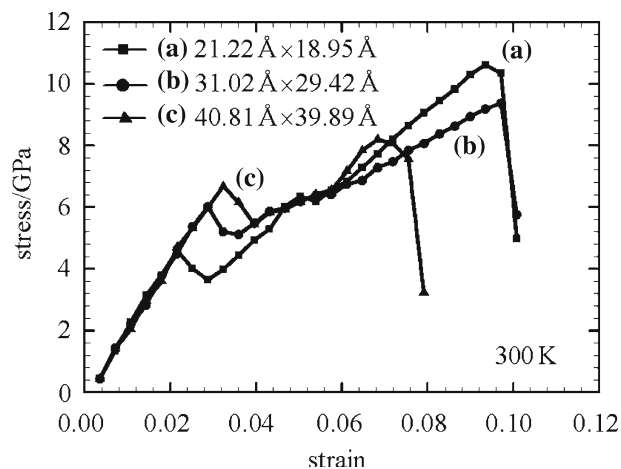
Fig. 7 Stress-strain response as a function of lateral dimensions at 300 K

significantly higher than the values for the bulk single-crystalline ZnO ($\sim$170 GPa at 300 K). This effect can be attributed to the stress induced by surfaces. Specifically, the lower coordination and in-plane contraction of the surfaces result in a tensile surface stress state and a compressive internal stress state in the interior of the belts. For deformation to occur, an applied stress has to overcome the internal compressive stress. This additional stress, which is negligible in bulk materials and is very high in nanowires, is primarily responsible for the much higher Young's modulus seen in Fig. 7 over the corresponding bulk value.

Young's modulus in Fig. 7 is size-dependent. As the lateral dimensions increase from 21.22 Å × 18.95 Å to 40.81 Å × 39.89 Å, decrease of $\sim$33% in Young's modulus is observed. The above trend can be explained by the fact that the surface-stress-induced internal compressive stress is inversely proportional to the lateral dimensions of the nanobelts [21, 29–31]. Specifically, the compressive stress can be expressed as

$$\sigma_C = \frac{2(f_1 + f_2)d}{d^2} = \frac{2(f_1 + f_2)}{d}, \qquad (6)$$

where f_1 and f_2 are the tensile surface stresses on $(2\bar{1}\bar{1}0)$ and (0001) surfaces, respectively, and $d = \sqrt{d_1 d_2}$ is the effective size of the nanobelt, with d_1 and d_2 being the lateral dimensions of the belts (Fig. 8(a)). The surface stresses for most materials are of the same order of magnitude as the corresponding surface energy values [29]. For ZnO, f_1 and f_2 are of the order of 2 N/m [32]. Figure 8(b) shows the approximate magnitude of the internal stress as a function of size. As the effective size decreases from 100 Å to 20 Å, a three-fold increase in the internal compressive stress is seen, sug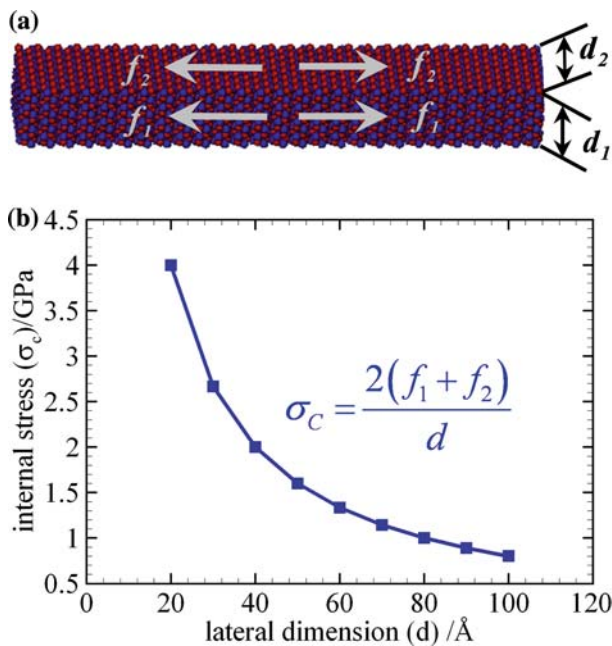gesting a significant size effect exists. It is this size effect that is responsible for the higher Young's modulus seen on the nanoscale. As the lateral dimensions increase, this effect diminishes and material properties approach their bulk values.

The effect of temperature on tensile behavior is also analyzed. As temperature increases from 300 K to 1 000 K, a softening trend is observed (Fig. 9). In particular, the elastic modulus decreases by 7.6%, 10.3% and 17%, respectively, for the 21.22 Å × 18.95 Å, 31.02 Å × 29.42 Å and 40.81 Å × 39.89 Å belts over the temperature range analyzed (see Fig. 10 and Table 1). The lower stiffness values at higher

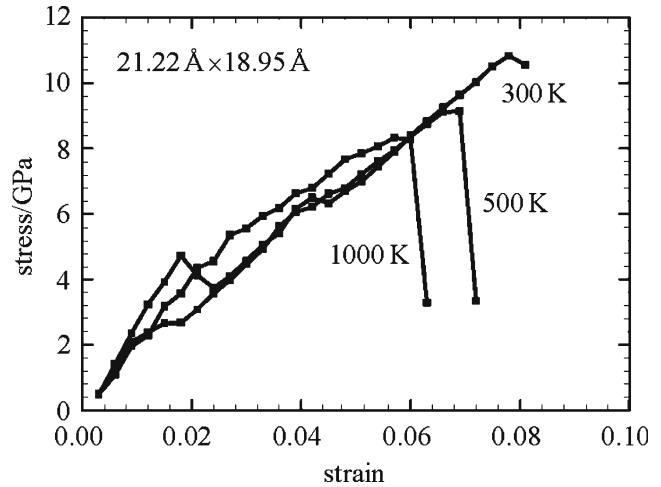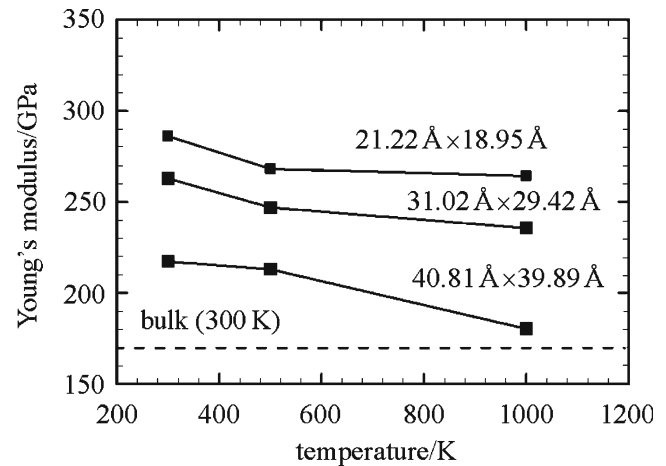**Fig. 9** Stress-strain curves at different temperatures for a 21.22 Å × 18.95 Å belt

Fig. 10 Young's modulus as a function of temperature for belts of three sizes along with the bulk value at 300 K

Table 1 Variation of Young's modulus with temperature and lateral dimensions of the nanobelts (values are in GPa)

Temperature/K	Lateral dimension		
	21.22 Å×18.95 Å	31.02 Å×29.42 Å	40.81 Å×39.89 Å
300	286.08	262.88	217.34
500	268.13	246.88	213.03
1 000	264.32	235.67	180.23

Fig. 8 (a) Tensile surface stresses; (b) Estimated internal compressive stress as a function of lateral dimensions

temperatures are due to changes in the equilibrium lattice spacing with temperature. Specifically, the increase of lattice parameters *a* and *c* with temperature and the nonlinearity of interatomic interactions cause the observed decrease in stiffness.

3.3 Thermal conductivity and effect of surface scattering of phonons

The thermal conductivity of the nanobelts over 300-1000 K is calculated according to Eq. (4). Figure 11 shows the variation of the calculated values with delay time. Short delay times ($\tau_m < 2$ ps) correspond to only very small temperature changes associated with thermal conduction, thus limiting the accuracy of the calculation and allowing random heat fluctuations to significantly affect the evaluation. The increasing trend of calculated conductivity values for this regime of delay time in Fig. 11 reflects this inaccuracy. On the other hand, long delay times ($\tau_m > 5$ ps) reduce the number of time origins available for averaging since the simulation time window is finite, causing statistical errors to increase. Because of the above factors, the intermediate delay time regime of $2 < \tau_m < 5$ ps is found to give a good balance between the different constraints. The profiles in Fig. 11 show a plateau of relative constant calculation results in this regime. The average value over this regime is taken as the thermal conductivity of the nanobelts for the conditions analyzed.

Figure 12 shows the thermal conductivity for nanobelts of different lateral sizes. First, we note that the values are between 3–15 W/(m·K) which is an order of magnitude lower than that for bulk ZnO ($\sim$100 W/(m·K)) [33]. The significant difference seen here is primarily associated with the high surface-to-volume ratios of the nanobelts. Specifically, the relatively large fractions of surface atoms significantly enhance surface scattering of phonons and decrease the phonon mean
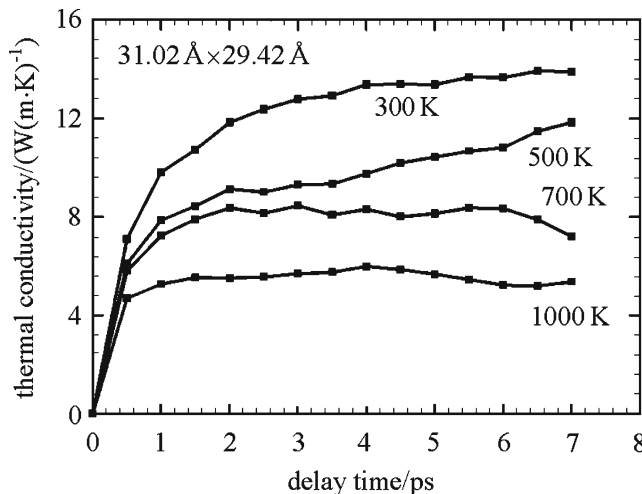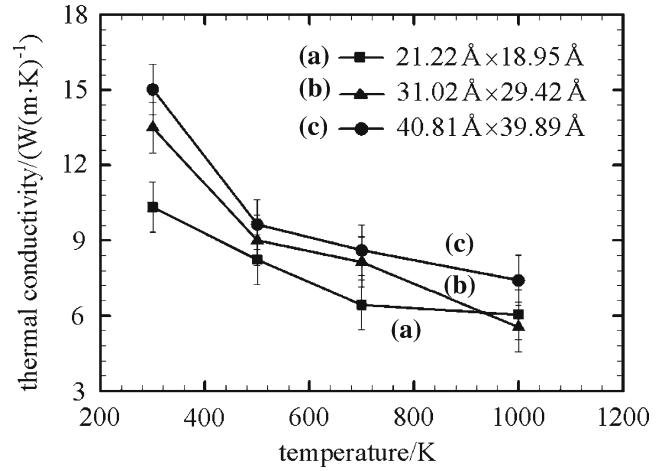

Fig. 12 Thermal conductivity as a function of lateral size and temperature

free path. The kinetic theory of fluids relates thermal conductivity *k* to the phonon mean free path Λ through

$$k = \frac{1}{3}C_v v \Lambda, \tag{7}$$

where C_v is specific heat and v is the velocity of heat carriers (for ZnO, the heat carriers are phonons and hence v represents the average phonon group velocity). Obviously, thermal conductivity is approximately proportional to the mean free path. Under conditions that phonon-phonon and phonon-defect interactions are negligible, the phonon mean free path can be expressed as [34]

$$\Lambda = \frac{d}{(1-p)}, \tag{8}$$

where *p* is the probability of specular scattering (which is a function of surface roughness and temperature) and *d* is the effective size of the nanobelt. For a body with perfectly specular (atomically smooth) surfaces, $p = 1$, consequently the mean free path and hence the thermal conductivity are not affected by boundary scattering. On the other hand, for a body with perfectly diffuse surfaces, $p = 0$, consequently the mean free path is equal to the size of the nanobelt i.e., $\Lambda = d$. In the nanobelts, the specularity value is between the limiting cases ($0 < p < 1$) and depends significantly on the surface attributes. Surface reconstructions discussed earlier modify surface atomic arrangement (Fig. 3), alter the surface scattering behavior of phonons, and reduce the specularity. Also, as shown by Berman et al. [35], surface specularity decreases as an inverse power of temperature, especially at higher temperatures. Consequently, the nanobelt surfaces are never perfectly specular and the mean free path is limited by the lateral dimensions of the belts. To state differently, the mean free path in the nanobelts is much smaller than that in bulk materials, effectively causing the observed size effect in thermal conductivity. In bulk materials, the characteristic length is much larger and the effect of boundary scattering of phonons is negligible, resulting in larger mean free paths and much higher conductivity values.
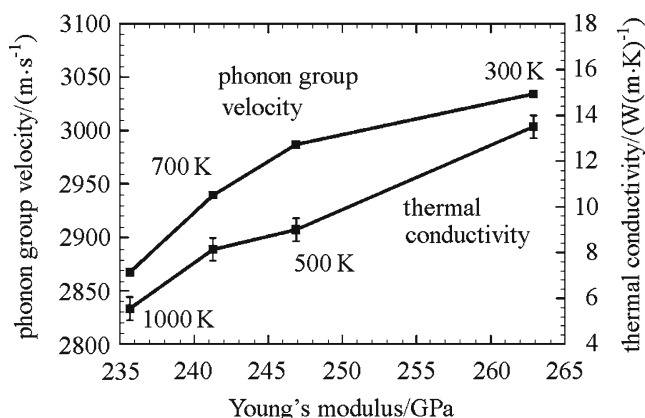

Fig. 11 Thermal conductivity of a 31.02 Å × 29.42 Å belt as a function of delay time at various temperatures between 300–1000 K

Fig. 13 Average phonon group velocity and thermal conductivity of a 31.02 Å × 29.42 Å belt as functions of Young's modulus

The effect of size on thermal conductivity can be clearly seen in Fig. 12. Over the temperature range of 300–1000 K, the conductivity of the 21.22 Å × 18.95 Å belt is approximately 11% lower than that of the 31.02 Å × 29.42 Å belt and the conductivity of the 31.02 Å × 29.42 Å belt is approximately 11.8% lower than that of the 40.81 Å × 39.89 Å belt. The trend observed here results directly from the higher surface-to-volume ratios and smaller mean free path at the smaller sizes.

The results in Fig. 12 also show that thermal conductivity decreases as temperature increases for all belt sizes analyzed. Specifically, between 300 K and 1000 K (the melting temperature of ZnO is 2250 K), decreases on the order of 50% in thermal conductivity are observed. This temperature effect can be attributed to thermal softening of the material and higher frequency phonon interactions at higher temperatures. The lower elastic stiffness of lattices at higher temperatures (which results from the nonlinearity of interatomic interactions) correspond to lower average phonon group velocities and lower levels of heat flux (see Fig. 13). Also at higher temperatures, higher frequency acoustic and optical phonon interactions become appreciable, leading to smaller mean free path and lower conductivity values [36]. The decrease in specularity is also partly responsible for decreases in thermal conductivity over the temperature range analyzed, as discussed earlier.

4 Conclusions

MD simulations have allowed the quantification of the effects of size and temperature on the elastic modulus and thermal conductivity of ZnO nanobelts with lateral dimensions between 21.22 Å × 18.95 Å and 40.81 Å × 39.89 Å. The size effects are due to the 1D structures and the high surface-to-volume ratios of the nanobelts at the size scale analyzed. The surface dominance of behaviors occurs through two mechanisms. The mechanism giving rise to the size effect on mechanical behavior is due to surface-stress-induced internal compressive stress which is inversely proportional

to the lateral dimensions. The mechanism giving rise to the size effect on thermal conduction is due to enhanced surface scattering of phonons which reduces the mean free paths and is affected by surface specularity. The enhanced surface scattering of phonons results from smaller interlayer spacings near surfaces and in-plane contractions of interatomic distances on surface planes. The elastic modulus and the thermal conductivity are also found to be significantly temperature-dependent over the temperature range of 300–1000 K. This dependence is due to the change of equilibrium lattice spacing with temperature and the nonlinearity of interatomic interactions. A correlation is obtained between the Young's modulus, phonon group velocity, and the thermal conductivity over the temperature range analyzed. The following characterizations have resulted from the analysis described here.

(1) The Young's moduli for the nanobelts with lateral dimensions 21.22 Å×18.95 Å, 31.02 Å×29.42 Å and 40.81 Å× 39.89 Å analyzed are 68.2%-27.8% higher, respectively, than the values for the corresponding values for bulk ZnO;

(2) When lateral dimensions increase from 21.22 Å×18.95 Å to 40.81 Å × 39.89 Å, an approximately 33% decrease in the Young's modulus is observed;

(3) Over the temperature range of 300 K to 1000 K, the Young's modulus decreases 7.6%, 10.3% and 17%, respectively, for the 21.22 Å×18.95 Å, 31.02 Å×29.42 Å and 40.81 Å × 39.89 Å belts;

(4) The thermal conductivity values for the nanobelts (3-15 W/(m·K)) are one order of magnitude lower than the corresponding value for bulk ZnO single crystal (∼100 W/(m·K));

(5) Over 300–1000 K, the conductivity of the 21.22 Å × 18.95 Å belt is approximately 31%-18% lower than that of the 40.81 Å × 39.89 Å belt;

(6) For the lateral sizes studied, an average decrease on the order of 50% in thermal conductivity is observed when temperature changes from 300 K to 1000 K.

References

1. Wang, Z.L., Kong, X.Y., Ding, Y., Gao, P. X., Hughes, W. L., Yang, R., Zhang, Y.: Semiconductiong and piezoelectric oxide nanostructures induced by polar surfaces. Advanced Functional Materials. **14,** 943–956 (2004)

2. Arnold, M.S., Avouris, P., Pan, Z.W., Wang, Z.L.: Field-effect transistors based on single semiconducting oxide nanobelts. Journal of Physical Chemistry. **107,** 659–663 (2003)

3. Bai, X.D., Gao, P.X., Wang, Z.L., Wang, W.G.: Dual-mode resonance of individual ZnO nanobelts. Applied Physics Letters. **82,** 4806–4808 (2003)

4. Comini, E., Faglia, G., Sberveglieri, G., Pan, Z.W., Wang, Z.L.: Stable and highle sensitive gas sensors based on semiconducting oxide nanobelts. Applied Physics Letters. **81,** 1869–1871 (2002)

5. Gao, P.X., Lao, C.S., Hughes, W.L., Wang, Z.L.: Three-dimensional interconnected nanowire networks of ZnO. Chemical Physics Letters. **408**, 174–178 (2005)

6. Gao, P.X., Wang, Z.L.: Nanoarchitectures of semiconducting and piezoelectric zinc oxide. Journal of Applied Physics. **97**, 044304 (2005)

7. Hughes, W.L., Wang, Z.L.: Nanobelts as nanocantilevers. Applied Physics Letters. **82**, 2886–2888 (2003)

8. Kong, X.Y., Wang, Z.L.: Spontaneous polarization-induced nanohelixes, nanosprings, and nanorings of piezoelectric nanobelts. Nano Letters. **3**, 1625–1631 (2003)

9. Wang, Z.L.: Zinc oxide nanostructures: Growth, properties and applications. Journal of Physics: Condensed matter. **16**, R829–R858 (2004)

10. Wang, Z.L.: Self-assembled nanoarchitectures of polar nanobelts/nanowires. Journal of Materials Chemistry. **15**, 1021-1024 (2005)

11. Wang, Z.L.: Functional oxides nanobelts-materials, properties and potential applications in nanosystems and biotechnology. Annual Review of Physical Chemistry. **55**, 159–196 (2004)

12. Kulkarni, A.J., Zhou, M., Ke, F.J.: Orientation and size dependence of the elastic properties of ZnO nanobelts. Nanotechnology. **16**, 2749–2756 (2005)

13. Shi, L., Hao, Q., Yu, C., Mingo, N., Kong, X., Wang, Z.L.: Thermal conductivities of individual tin dioxide nanobelts. Applied Physics Letters. **84**, 2638–2640 (2004)

14. Pan, Z.W., Dai, Z.R., Wang, Z.L.: Nanobelts of semiconducting oxides. Science. **291**, 1947–1949 (2001)

15. Picu, R.C., Borca-Tasiuc, T., Pavel, M.C.: Strain and size effects on heat transport in nanostructures. Journal of Applied Physics. **93**, 3535–3539 (2003)

16. Binks, D.J. Computational modelling of zinc oxide and related oxide ceramics. [Ph.D. thesis], University of Surrey, Harwell, 1994.

17. Binks, D.J., Grimes, R.W.: Incorporation of monovalent ions in ZnO and their influence on varistor degradation. Journal of the American Ceramic Society. **76**, 2370–2372 (1993)

18. Demontis, P., Spanu, S., Suffritti, G.B.: Application of the wolf method for the evaluation of Coulombic interactions to complex condensed matter systems: Aluminosilicates and water. Journal of Chemical Physics. **114**, 7980–7988 (2001)

19. Wolf, D., Keblinski, P., Phillpot, S.R., Eggebrecht, J.: Exact method for the simulation of Coulombic systems by spherically truncated, pairwise r^{-1} summation. Journal of Chemical Physics. **110**, 8254–8282 (1999)

20. Zhou, M.: A new look at the atomic level virial stress: On continuum-molecular system equivalence. Proceedings of the Royal Society of London. **459**, 2347–2392 (2003)

21. Sander, S.: Surface stress: Implications and measurements. Current Opinion in Solid State and Materials Science. **7**, 51–57 (2003)

22. Olson, G.B., Cohen, M.: Theory of martensitic nucleation: A current assessment In: Aaronson, H., Laughlin, D.E., Sekerka, R.F., Wayman, C.M. (eds.) Proc. Intl. Conf. Solid-Solid Phase Transformations, Pittsburgh: AIME, 1145–1164, 1982

23. Nakanishi, N., Nagasawa, A., Murakami, Y.: Lattics instability and soft modes. Proc. ICOMAT-82 Journal de Physique. **43**, C4 35–55 (1982)

24. Olson, G. B., Cohen, M.: Classical and nonclassical mechanisms of martensitic transformation. Proc. ICOMAT-82 Journal de Physique. **43**, C4 75–88 (1982)

25. Mendelson, S.: The soft mode criterion for martensitic transformations. Proc. ICOMAT-82 Journal de Physique. **43**, C4 139–144 (1982)

26. Kriven, W.M.: Shear transformations in inorganic materials In: Aaronson, H., Laughlin, D.E., Sekerka, R.F., Wayman, C.M. (eds.) Proceedings of the International Conference on Solid to Solid Phase Transformations, Pittsburgh: AIME, 1507–1532, 1982

27. Geuenin, G., Gobin, P.F.: Localized lattice instability related to the nucleation problem of martensite. Proc. ICOMAT-82 Journal de Physique. **43**, (1982)

28. Clapp, P.C., McLaughlin, D.: Molecular dynamics simulation of martensitic nucleation. In: Proc. of the Int. Conf. on Martensitic Transformations (ICOMAT). 322–344, 1980

29. Diao, J., Gall, K., Dunn, M.L.: Surface-stress-induced phase transformation in metal nanowires. Nature Materials. **2**, 656–660 (2003)

30. Gall, K., Diao, J., Dunn, M.L.: The strength of gold nanowires. Nano Letters. **4**, 2431–2436 (2004)

31. Liang, W., Zhou, M.: Pseudoelasticity of single crystalline cu nanowires through reversible lattice reorientations. Journal of Engineering Materials and Technology. **127**, 123–133 (2005)

32. Jiang, X., Jia, C.L., Szyszka, B.: Manufacture of specific structure of aluminum-doped zinc oxide films by patterning the substrate surface. Applied Physics Letters. **80**, 3090–3092 (2002)

33. Wolf, M.W., Martin, J.J.: Low temperature thermal conductivity of zinc oxide. Physica Status Solidi. **17**, 215–220 (1973)

34. Zou, J., Balandin, A.: Phonon heat conduction in a semiconductor nanowire. Journal of Applied Physics. **89**, 2932–2938 (2001)

35. Berman, R., Foster, E.L., Ziman, J.M.: Thermal conductivity in artificial sapphire crystals at low temperatures. I. Nearly perfect crystals. Proceedings of the Royal Society of London A. **231**, 130–144 (1955)

36. Joshi, Y.P., Tiwari, M.D., Verma, G.S.: Role of four-phonon processes in the lattice thermal conductivity of silicon from 300 to 1 300°k. Physical Review B. **1**, 642–646 (1970)